

Article

Not peer-reviewed version

Enhancing Conversion Efficiency of 3D-Printed Copper (I) Sulfide Thermoelectrics via Sulfur Infusion Process

[Raden Gustinvil](#) , William Jordan Wright , Giuseppe L. Di Benedetto , Donald Skelton , Samuel Stuart , John W. Drazin , [Emrah Celik](#) *

Posted Date: 10 August 2023

doi: 10.20944/preprints202308.0807.v1

Keywords: thermoelectricity; copper (I) sulfide; 3D printing; sulfur infusion; direct ink writing



Preprints.org is a free multidiscipline platform providing preprint service that is dedicated to making early versions of research outputs permanently available and citable. Preprints posted at Preprints.org appear in Web of Science, Crossref, Google Scholar, Scilit, Europe PMC.

Copyright: This is an open access article distributed under the Creative Commons Attribution License which permits unrestricted use, distribution, and reproduction in any medium, provided the original work is properly cited.

Article

Enhancing Conversion Efficiency of 3D-Printed Copper (I) Sulfide Thermoelectrics via Sulfur Infusion Process

Raden Gustinvil ¹, William Jordan Wright ¹, Giuseppe L. Di Benedetto ², Donald Skelton ², Samuel Stuart ³, John Drazin ⁴ and Emrah Celik ^{1,*}

¹ Mechanical and Aerospace Engineering Department, University of Miami, FL 33146, USA

² U.S. Army Combat Capabilities Development Command Armaments Center, Picatinny Arsenal, NJ 07806, USA

³ U.S. Navy Naval Surface Warfare Center, Crane Division, IN 47522, USA

⁴ Air Force Research Laboratory, Wright-Patterson Air Force Base, OH 45324, USA

* Correspondence: e.celik@miami.edu; Tel.: (+1-305-284-9364)

Abstract: Copper(I) sulfide (Cu_2S) is a low-cost, earth-abundant, and non-toxic thermoelectric material for applications in the middle-high temperature range (>650 K). Although 3D printing these materials can simplify their manufacturing, elevated temperatures observed during sintering impair their crystal structure and energy conversion efficiency. In this study, we demonstrated a novel post-processing methodology to revert the thermoelectric properties of the 3D printed Cu_{2-x}S materials back to the unimpaired state via sulfur infusion. After printing and sintering, sulfur was infused into the specimens under vacuum to optimize their crystal structure and achieve high thermoelectric efficiency. Chemical analysis and X-ray Diffraction (XRD) tests showed that after the sulfur infusion process, the Cu/S ratio was reverted close to the stoichiometric level. 3D printed Cu_{2-x}S showed p-type thermoelectric behavior with electrical conductivity peaking at $143 \text{ S}\cdot\text{cm}^{-1}$ at 750 K and Seebeck coefficient of $175 \mu\text{V}\cdot\text{K}^{-1}$ at 627 K. Figure of merit (ZT) value of 1.0 at 780 K was achieved which is the highest value ever reported for a 3D printed Cu_{2-x}S thermoelectrics at this temperature. Fabrication of environmentally friendly thermoelectric materials with extended dimensional freedom and conversion efficiency has the potential to impact the thermoelectric industry with new energy conversion applications and lowered manufacturing costs.

Keywords: thermoelectricity; copper (I) sulfide; 3D printing; sulfur infusion; direct ink writing

1. Introduction

The development of sustainable energy sources has become a growing industry as our dependencies on fossil fuels exceed the currently available supply. The increase in climate change is also primarily attributed to the use of these fossil fuels in the automotive and energy production sector [1]. To minimize the implications of the energy production and consumption systems, high-performance thermoelectric (TE) devices can be used to recapture the waste heat emitted during energy conversion. Thermoelectricity refers to the phenomena by which thermal energy is transformed directly into electrical energy (and vice versa) without any moving parts or working fluids. Thermoelectric generators (TEG) have several advantages over conventional energy sources including their simple design, silent operation, and minimal maintenance requirements [2]. The most common and widely used materials for commercial thermoelectric materials are bismuth telluride (Bi_2Te_3) [3–7] for room temperature applications and lead telluride (PbTe) [8–10] for middle-range temperature applications (~ 500 K) as numerous studies have reported ZT values near and exceeding one. Although these materials are commonly used in thermoelectric applications; tellurium is a rare earth element and highly toxic. Therefore, the use of these materials leads to high manufacturing costs and safety concerns. The search efforts to discover new thermoelectric materials are expanding rapidly to reduce these limitations and enhance the thermoelectric conversion efficiency of the existing materials.

The efficiency of thermoelectric materials is quantified by the dimensionless figure of merit (ZT) according to the following equation:

$$ZT = (S^2\sigma T)/\kappa \quad (1)$$

where S is the Seebeck coefficient, σ is the electrical conductivity, κ is the thermal conductivity and T is the absolute temperature (K). Therefore, thermoelectric materials with high energy conversion efficiency (ZT) must have a high Seebeck coefficient and electrical conductivity with minimal thermal conductivity. Phonon-glass electron crystal concept (PGEC) is a class of highly researched thermoelectric materials due to their high ZT level. These materials possess good electrical properties under crystalline structure and a low lattice thermal conductivity when exhibiting a disordered atomic arrangement. An extension of this principle is labeled the phonon-liquid- electron-crystal (PLEC) concept [11] where the material exhibits a liquid-type relationship with its ions, thus reducing the typically high thermal conductivity seen in crystalline semiconductors. Copper-based chalcogenides fit this category of materials. High ZT level, environmental friendliness, and earth abundancy make this class of materials a viable alternative to traditional thermoelectrics [12]. Within the class of copper chalcogenides, two are well known: copper selenide (Cu_2Se) and copper(I) sulfide (Cu_2S). Both compounds are p-type semiconductors with high ion mobility as copper vacancies act as acceptors. Cu_2Se has favorable thermoelectric performance in the temperature range of 700–900 K with low thermal conductivity. A high ZT of 2.1 was achieved in carbon dot doped Cu_2Se specimens where nanoparticle doping led to energy filtering along the grain boundaries and phonon scattering further reducing thermal conductivity [13]. Despite its impressive thermoelectric performance, Cu ion migration and Se evaporation have been observed when used at elevated temperatures for extended periods of time [14,15]. In addition, the cost of copper(I) sulfide is close to half that of copper selenide which is more practical for commercialization purposes [16].

Also known as chalcocite, copper(I) sulfide (Cu_2S) has three distinct stoichiometric phases. γ - Cu_2S (monoclinic $P21/c$ crystal structure below ~ 370 K), β - Cu_2S (hexagonal between ~ 370 –600 K), and α - Cu_2S (cubic above 600 K), which exhibit the thermoelectric properties of interest [17–20]. As a thermoelectric material, copper(I) sulfide has already proven to be a viable alternative with reported values of maximum ZT of 1.7 at 1000 K for bulk materials [21]. One drawback, however, is that Cu_2S has one of the most complex phase diagrams of a metal sulfide making it difficult to synthesize with stoichiometric accuracy [22] over the entire composition range to form a continuous solid solution. Copper(I) sulfide (Cu_2S) can be composed of various phases coexisting in different proportions at room temperature however at high temperatures a phase transformation occurs converting into a single cubic phase [23,24]. The thermoelectric properties of copper(I) sulfide are closely correlated to its stoichiometry. Above the superionic phase transition temperature (~ 350 K), the mobility of copper ions can promote copper surface migration under the right conditions which affects the conversion efficiency. This can be mitigated by either limiting the working current and/or introducing a grain-boundary engineered microstructure. Thus, allowing the flow of electrons/holes while blocking ion movement [25].

Traditional manufacturing of TE modules is a complex, multi-step process involving powder synthesis, sintering, leg dicing, metallization, and interconnect fabrication [7]. In addition to the fabrication complexity, current TE module manufacturing is limited to simple planar configurations and material waste is relatively high [26]. Other fabrication techniques such as chemical synthesis, hot pressing, spark sintering, and mechanical alloying have been used to study the thermoelectrical properties of Cu_2S . However, these methods also require high temperatures and pressures making them time and labor-intensive processes. Additive manufacturing (AM) is an alternative approach to expand the design space of these materials and minimize the limitations of conventional manufacturing techniques. AM of thermoelectric materials is of great interest to the scientific community as this offers the potential for custom TEG modules that meet specific energy generation requirements [27–29]. Prior studies have been focused on Bi_2Te_3 primarily in the form of spin coating [30], screen printing [31], or inkjet printing [32] with the work of Kim et al. [33] paving the way for the fabrication of shape conformal bulk Bi_2Te_3 samples with a max ZT of 0.9 @ 398 K. A pseudo direct ink writing (DIW) additive manufacturing process was recently used to additively manufacture Cu_2 -

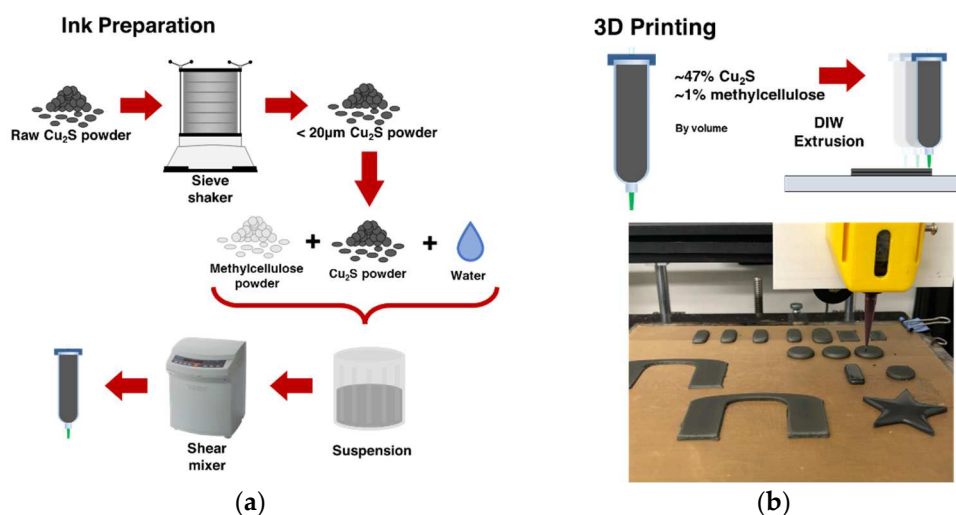
$\times S$ and a maximum ZT of ~ 0.63 @ 966 K was achieved [34]. Although this pioneering study proved tool-free fabrication of sulfur-based TE materials, the process needs to be improved and optimized to achieve ZT levels analogous to those of commercial materials.

This work presents an additive manufacturing methodology of $Cu_{2-x}S$ using DIW followed by a novel sulfur infusion post-processing technique. The DIW process was optimized to achieve geometrically complex structures with high ZT levels for these materials. Annealing was then performed in a sulfur-rich environment to bring back the lost sulfur into the fabricated material and achieve similar ZT levels of commercial TE materials for the first time. The fabrication of environment-friendly and earth-abundant materials has great potential to greatly impact the field of thermoelectricity. Along with high dimensional freedom, low cost, and high conversion efficiency this further expands its applications in energy harvesting and waste heat recovery.

2. Materials and Methods

2.1. Ink Preparation and 3D Printing

Copper (I) sulfide powders (Cu_2S) were purchased from American Elements (99.995% trace metals basis). As received powders were sieved using the Retsch AS 450 Control sieve shaker to obtain a size distribution of $< 20 \mu m$ and allow for maximum loading of the paste for direct ink writing. The material used for the paste was a mixture of water, methylcellulose (average MW $\sim 200\,000$, The CandleMakers Store), and copper (I) sulfide powder. Methylcellulose and copper (I) sulfide powders were incrementally added to water and mixed at 1300 rpm for 2 min in a high-shear planetary mixer (Thinky ARE 310). This process was repeated until the mixture contained $\sim 1\%$ methylcellulose and $\sim 47\%$ copper(I) sulfide by volume as shown in Figure 1a. After mixing, a 30-cc syringe was filled with the thermoelectric paste and an Ultimius V pressure regulator was used to extrude the material during the DIW process. An 840- μm tapered nozzle was used to print the paste at room temperature on a glass substrate lined with a Teflon sheet. Once the printing was completed, the printed structure was left in ambient air for 24 h to cure (Figure 1b).



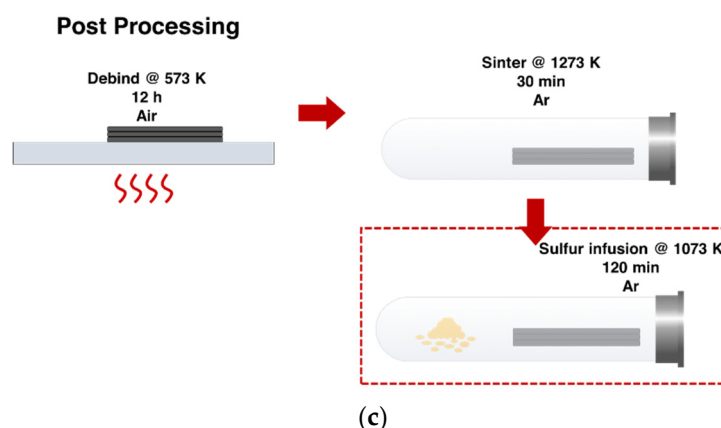


Figure 1. Schematic of the multi-step fabrication process applied to produce Cu_{2-x}S samples: (a) ink preparation, (b) 3D printing, and (c) post processing.

2.2. Sintering and Sulfur Diffusion Postprocessing

3D-printed specimens were placed in a muffle furnace at 573 K for 12 h in ambient air to remove the organic binder from the printed structures. Sintering was then performed at 1273 K for 30 min under vacuum. Prior to the vacuum application, the heating chamber was purged with argon gas to minimize the oxygen content in the chamber. Due to the high sintering temperature, sulfur within the alloy volatilizes making the sample super-saturated with copper. Copper precipitates can be found within and on the surface of the sample after the sintering process is completed. This reduces the overall thermoelectric properties of the sample. To diffuse the lost sulfur back into the system and enhance the thermoelectric performance, the sintered specimens underwent a post-processing procedure where the samples were heated at 1073 K for 2 h with sulfur powder (99.5%, Alfa Aesar) in the vacuum sealed furnace and purged with argon gas as shown in Figure 1c. The amount of sulfur powder used in post-processing was 5% of the total mass of the sample.

2.3. Characterization of Crystal Structure and Sulfur Content

Scanning electron microscopy (SEM) was conducted on sintered and post-processed samples. Images were taken on the Zeiss Gemini Field Emission SEM. Sputter coating commonly applied on SEM samples to minimize charging was not required due to the highly conductive nature of the samples. X-ray diffraction analysis (XRD) was performed on the Rigaku Smart Lab to characterize the crystal structure of the three sets of samples: 1) as supplied powder, 2) samples after sintering, and 3) samples after sintering and sulfur diffusion post-processing. In addition to XRD analysis to evaluate the effect of sulfur diffusion post-processing on the alloy morphology, sulfur content was also quantified using the LECO CS844 elemental analyzer following the methodology provided by the manufacturer. The device was calibrated prior to testing using 502-085 zinc sulfide reference material supplied by LECO.

2.4. Thermoelectric Characterization

Electrical conductivity and Seebeck coefficient of the 3D printed specimens were measured using the Linseis LSR-3 system. Electrical conductivity was calculated using the measured resistivity of the sample via the four-point probe method where a constant current was applied through the upper and lower electrode and the voltage drop was recorded in the middle of the sample between two thermocouples. Simultaneously, the Seebeck coefficient measurement was conducted using an upper and lower thermal gradient of 30 K which was maintained using gradient heaters. The voltage and temperature differential were probed and recorded in the middle of the sample approximately 3 mm apart using the same platinum-coated thermocouples. All measurements were performed from room temperature to 774 K in a helium (He) environment as shown in Figure S2.

Thermal conductivity (κ) of the 3D printed thermoelectric materials was calculated according to the following equation:

$$\kappa = D \cdot C_p \cdot \rho \quad (2)$$

where D is thermal diffusivity, C_p is specific heat and ρ is the mass density. Prior to the thermal diffusivity measurements, samples were cut to 10 mm OD x 2 mm thickness and were sanded to achieve parallel contact surfaces. Sample dimensions were measured with a micrometer within $\pm 1 \mu\text{m}$ accuracy. Thermal diffusivity (D) was performed on a Netzsch LFA 427 unit (Selb, Germany) using a 10 mm graphite holder in 100 K increments up to 774 K under the helium flow of 150 mL/min. The laser was operated at 700 V with a 0.5 ms pulse width and collected in an Indium antimonide (InSb) cryogenically cooled detector. The standard model with a linear background was used to fit the data to calculate the half time. A Netzsch DSC 404 unit (Selb, Germany) was used to calculate the C_p of the samples up to 774 K using the C_p ratio method with sapphire as the standard in 50 mLmin⁻¹ flowing Ar heated at 5 Kmin⁻¹ in a platinum crucible. The sensitivity was calibrated against metal melting in platinum crucibles with an alumina liner. A constant value of 30 ppmK⁻¹ was used for the CTE from room temperature to 774 K for all samples. Thermal diffusivity and specific heat measurement are given in Supplementary Figure S3. Densities (ρ) of the 3D printed parts were calculated using their geometrical dimensions and mass at room temperature and assumed to be unchanged as a function of temperature for the thermal conductivity calculations.

3. Results and Discussion

3.1. Structural and Morphological Analysis

Using the DIW technique, various complex geometry could be fabricated which would be extremely difficult and/or costly to achieve via traditional manufacturing. As shown in Figure 2, shape conformality for thermoelectric legs becomes feasible paving the way for unconventional TEG designs such as annular or unileg form factors. Lattice structures (Figure 2b) were also fabricated demonstrating the enhanced design freedom of direct ink writing process compared to the conventional manufacturing technologies.

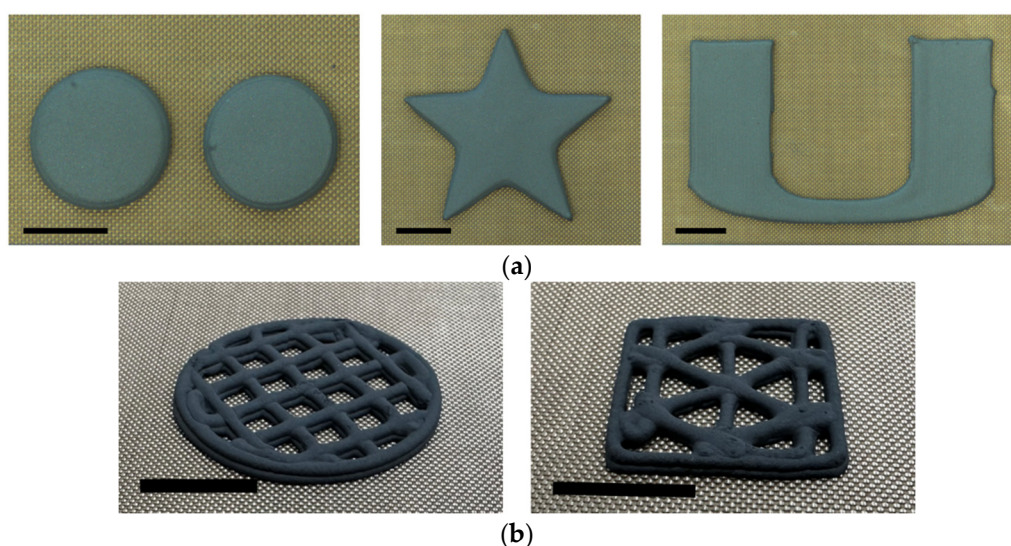


Figure 2. 3D geometries capable of being produced using DIW methodologies: (a) solid geometries and (b) lattice structures. Scale bars, 10 mm.

Optical microscope images were taken of the 3D printed samples to observe the change in microstructure. Air-cured samples were imaged as-is due to the delicate nature of the specimens. Sintered and sulfur-infused samples were encased using a hot mounting press in clear acrylic and polished for cross-sectional analysis. As shown in Figure 3b after sintering copper precipitates from

the solid solution within and on the surface of the sample due to the volatilization of sulfur. After the reintroduction of sulfur, some copper particles remain but they are greatly reduced in size as the precipitates are reabsorbed in the copper(I) sulfide solid solution (Fig 3c).

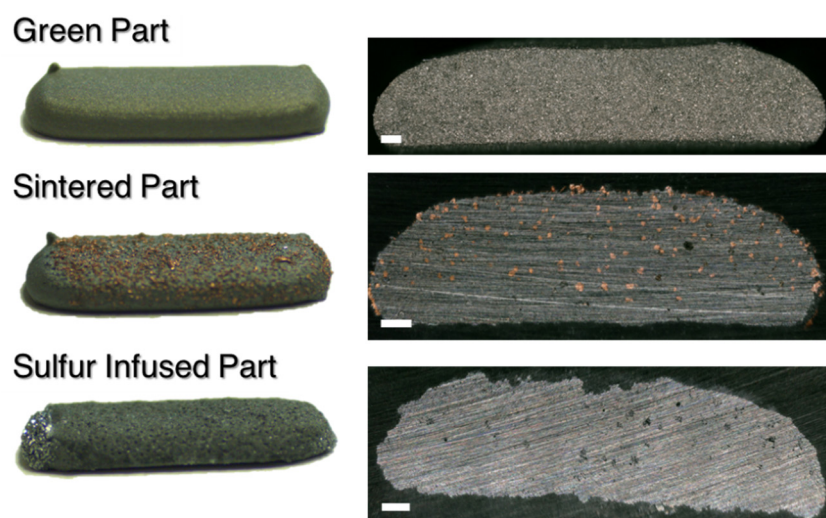
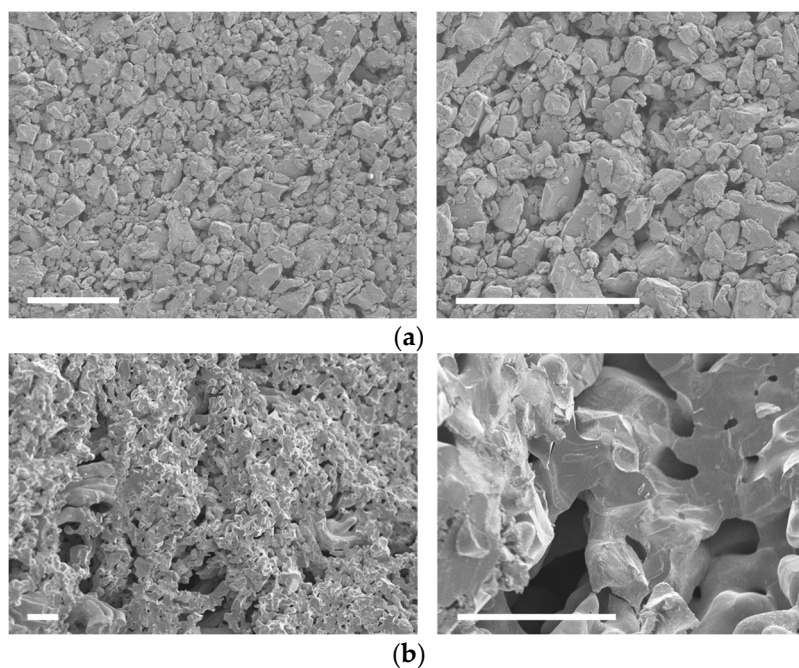


Figure 3. Direct ink writing (DIW) 3D printed samples air cured, sintered, and post sulfur infusion process along with accompanying cross-section. Scale bars, 500 μm .

SEM imaging was conducted on the copper(I) sulfide samples at various stages of the manufacturing process. As shown in Figure 4a and 4b the powder granules are clearly visible as individual entities in the samples after 3D printing and curing for 24 h at room temperature. The structural integrity of the printed specimens was achieved by simply using methylcellulose powder and water which keeps the Cu_2S particles together in these samples. These samples prior to the sintering step are referred to as green parts.



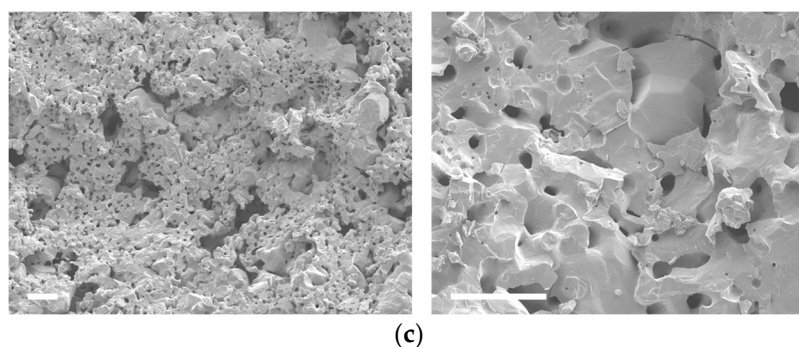


Figure 4. SEM of thermoelectric samples a) after printing and room temperature curing, b) after high-temperature sintering, and c) after the sulfur infusion postprocessing. Scale bars, 50 μm .

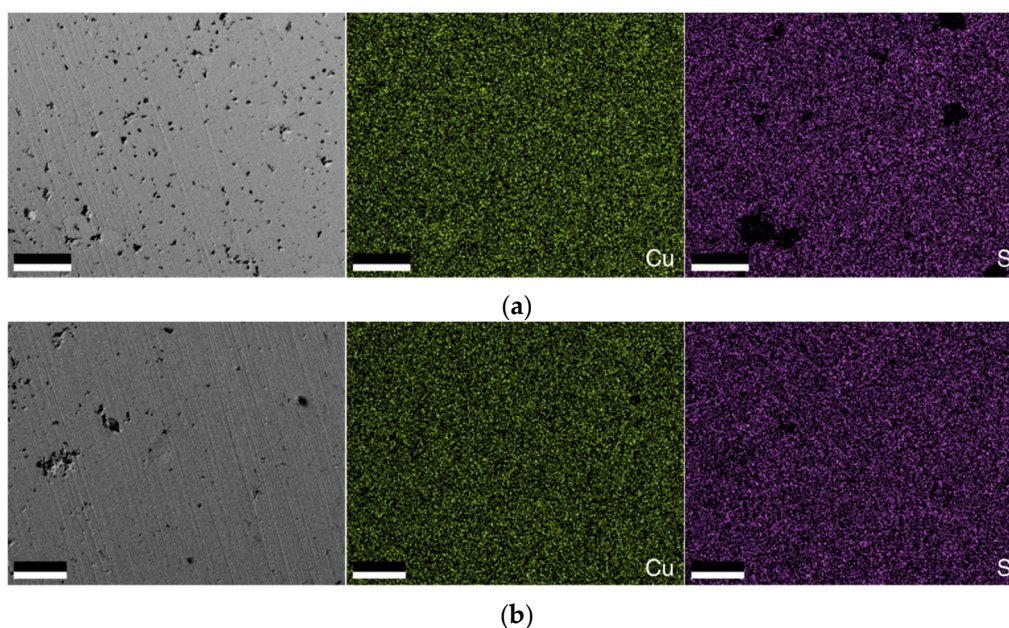


Figure 5. SEM imaging of a randomly selected area, with respecting element mapping of Cu and S for (a) sintered samples and (b) postprocessed samples. Scale bars, 200 μm .

The sintering temperature was chosen to be 1273 K after performing temperature optimization based on the structural integrity, form retention of the samples (i.e., the tendency of the samples to warp or deform during sintering), and thermoelectric performance. It is hypothesized that the selection of too high a sintering temperature would lead to loss of the original printed form factor along with an increase in the thermal conductivity due to decreased phonon scattering thus decreasing overall TE performance. Similarly, too low of a sintering temperature would result in insufficient melting and therefore powder granules would not properly coalesce to form mechanically solid samples. This would also decrease the electrical conductivity as an interconnected network is not properly formed within the samples. During the sintering process performed at 1273 K, the binding agent decomposes leaving a large amount of porosity as shown in Figure 4c-e. The pores are generally uniform with a size of nearly 10 μm in diameter. Sintering also results in partial melting and coalescing of the individual Cu_2S granules enhancing the structural integrity and TE properties of the fabricated specimens. Sulfur infusion post-processing performed on the sintered specimens does not lead to any notable morphological changes as shown in Figure 4.

Densities of the green, sintered and post processed specimens are given in Table 1. During the thermal debinding process, the binding agent (methylcellulose and water) is volatilized leaving behind pores in the sample. Between the thermal debinding and sintering process, samples uniformly shrunk by $19.01\% \pm 4.71\%$. Compression testing was performed on an Instron 5564 universal test setup (1kN load cell) using a testing strain rate of 0.5 mm/min parallel to the build direction. The data is shown

in Figure 6. The compressive strength was evaluated at 15% strain resulting in a compressive strength of 8.3 MPa, 21.7 MPa, and 33.7 MPa for as-printed, sintered, and post-processed samples, respectively. This is comparable to bulk values in literature for commercially used $\text{Bi}_{0.5}\text{Sb}_{1.5}\text{Te}_3$, commonly found in TE modules [35].

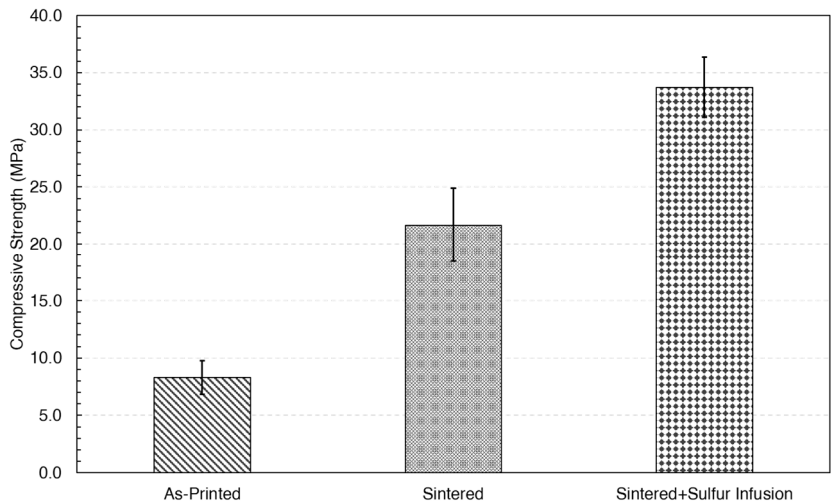


Figure 6. Compressive strength at various stages of DIW fabricated samples.

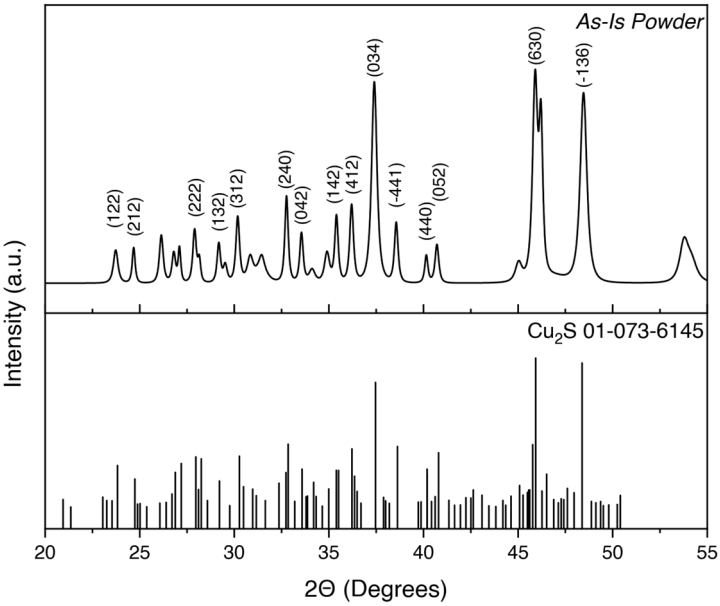
Table 1. Volumetric density of copper(I) sulfide samples after printing, after sintering, and after the sulfur infusion process.

Sample ID	Density (g/cm³)	STD	Relative Density
Printed Part	2.79	0.07	49.9
Sintered	2.84	0.05	50.8
Post-Processed	2.68	0.13	47.8

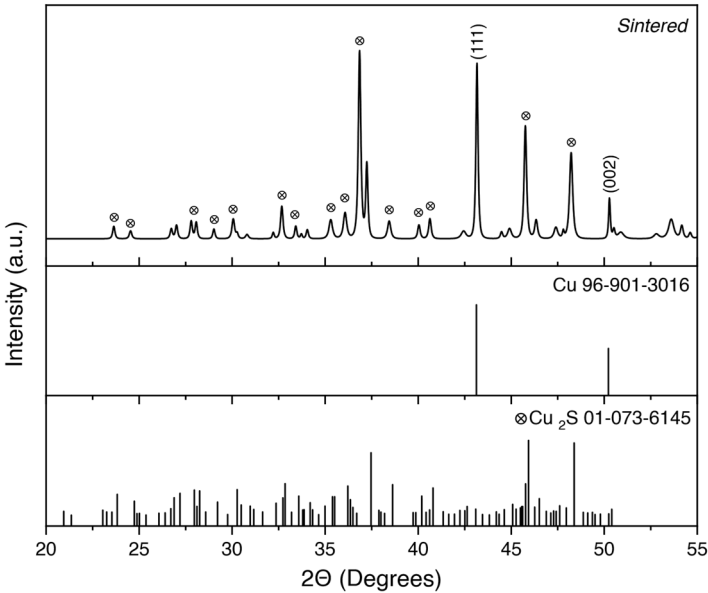
Literature value for bulk density of Cu_2S : 5.6 g/cm³ [36].

3.2. Compositional Analysis

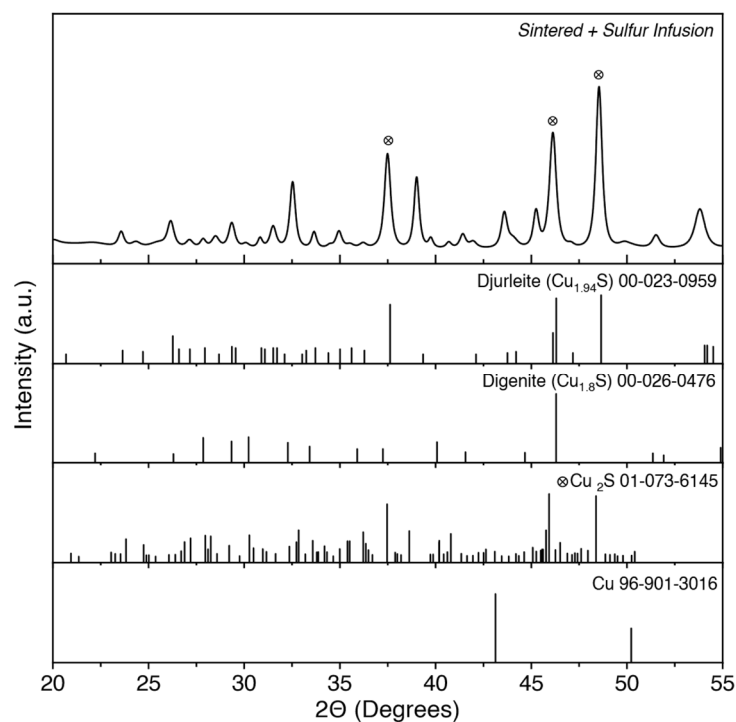
Powder XRD was performed on as received powder and on 3D printed parts (after sintering and after the sulfur infusion process) to observe the alterations in the chemical structure of Cu_{2-x}S specimens in the sintering and post-processing steps. Prior to the XRD analysis, 3D printed samples were ground into a homogenous powder using a mortar and pestle. The XRD pattern data for the Cu_2S powder as received from the manufacturer is shown in Figure 7a. According to these results, the precursor material was in close agreement with monoclinic Cu_2S (ICDD 01-073-6145) which is expected with minimal impurities present. Figure 7b presents the pattern data for Cu_{2-x}S samples after sintering at 1273 K for 30 min. Strong Cu peaks are observed since sulfur volatilizes during the sintering process, allowing for the migration of free copper ions to the surface of the samples. The same phenomenon has been reported to occur in literature [37]. After the sulfur infusion process, however, the Cu peaks are no longer as prominent as shown in Figure 7c indicating the reabsorption of the free Cu into the material.



(a)



(b)



(c)

Figure 7. XRD data of (a) Cu₂S as-is powder, (b) sintered sample, and (c) sintered + sulfur infused sample.

Figure 8 further supports the conclusions drawn in XRD results where the compositional weight percentages of sulfur in the samples were measured by the LECO CS844 analyzer. As shown in this figure, as-received powder has a weight percentage of $18.89\% \pm 0.24\%$ which is expected for stoichiometric Cu₂S. There is a significant decrease in sulfur content to the weight percentage of $14.91\% \pm 0.05\%$ after sintering was conducted at 1273 K. At this sintering temperature, sulfur may volatilize creating a copper excess mixture within the sample. After the sulfur infusion post-processing was performed, the sulfur weight percentage was elevated to $19.33\% \pm 0.36\%$ effectively making the sample sulfur rich. The difference in sulfur composition between the raw powder and post processed sample is statistically significant, evidencing that sulfur rich alloy was produced after the sulfur-infusion process was performed. To ensure a homogenous solid solution was fabricated x-ray mapping using scanning electron microscopy of the elemental distribution was performed as shown in Figure 5. The bottom row represents the postprocessed samples and shows that the distribution between Cu and S is homogeneous over the area pictured compared to the top row where Cu precipitates are clearly visible in the sintered samples when comparing Figure 5c to Figure 5e. The two images below show no sign of Cu precipitates.

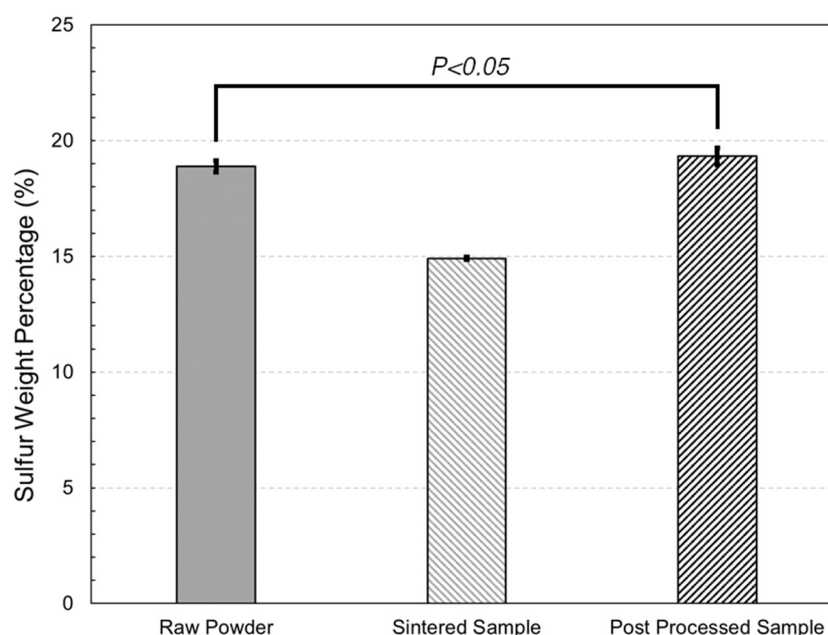


Figure 8. Variation of sulfur compositional at different stages of the fabrication process.

3.3. Thermoelectric Characterization

Figure 9 displays the electrical conductivity (σ), Seebeck coefficient (S), thermal conductivity (κ), and figure of merit (ZT) of sintered and sulfur infused (post-processed) Cu_{2-x}S samples in the temperature range from 300 – 800 K. For only sintered samples, the electrical conductivity ranged from 3-16 Scm^{-1} (Figure 9a). For sulfur-infused specimens, however, there was a significant increase in electrical conductivity ranging from 35-143 Scm^{-1} . This can be attributed to the change in the material composition during the sulfur infusion process as explained in the previous section. As reported previously by Sorokin [38], copper-rich Cu_{2-x}S has very low electrical conductivity compared to sulfur-rich Cu_{2-x}S . The slight difference in the Cu/S ratio can present large variations in electrical conductivity due to differences in mobility. The effect of transitioning from copper-rich to sulfur-rich material can be so dramatic that the electrical conductivity increases four orders of magnitude as reported in this study. The variation of the Seebeck coefficient as a function of temperature is given in Figure 9b where higher Seebeck coefficients were reported for copper-rich (sintered) specimens compared to the sulfur-infused samples. The trend in Seebeck coefficient versus sulfur deficiency is the inverse to that seen in electrical conductivity. This is due to the fact that the Seebeck coefficient is inversely correlated to carrier concentration, while electrical conductivity is directly correlated, as reported previously [39]. Sintered samples had S values ranging from 103-280 μVK^{-1} while post-processed samples ranged from 103-175 μVK^{-1} . As the Cu/S ratio increases (observed in only sintered samples), the samples tend to behave more insulator-like with a higher Seebeck coefficient and lower electrical conductivity [17].

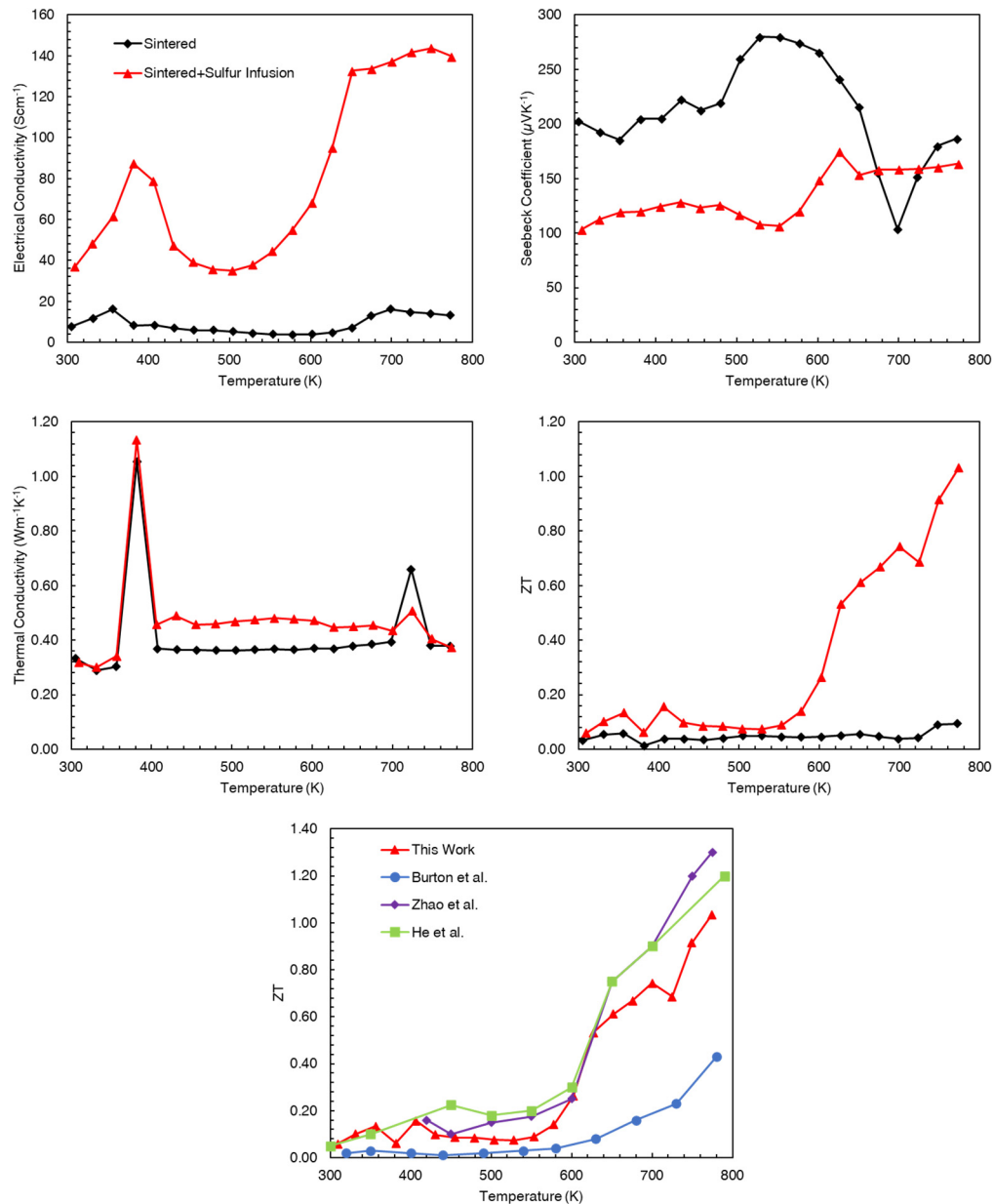


Figure 9. Thermoelectric properties of 3D printed Cu_{2-x}S samples: electrical conductivity, Seebeck coefficient, thermal conductivity, and figure of merit ZT , and figure of merit compared to other values in recorded literature [19,21,34].

To assess the effect of material stability at elevated temperature test conditions, the thermoelectric characterization cycle was repeated three times. Subsequent testing of the samples indicated slightly degraded performance after each cycle (**Figure S1**) with a decrease in electrical conductivity and an increase in Seebeck coefficient. This can be attributed due to the gradual loss of sulfur during the high temperature segment of the testing cycle. Thermal conductivity results are given in Figure 9c. The thermal conductivities of both sintered and sulfur-infused samples are in the range of 0.4 to 0.7 $\text{W m}^{-1}\text{K}^{-1}$ (Figure 8c). Post-processed specimens mark a slightly higher thermal conductivity level than sintered samples level. The rapid jumps in the thermal conductivity plot are propagations from the specific heat data and these are most likely due to phase changes observed at those temperature points. Compared to the literature results for fully dense samples ($\kappa \sim 0.3 - 0.6 \text{ W m}^{-1}\text{K}^{-1}$ @ RT)[40], the values recorded here follow the same trend as expected. The average pore area was $\sim 106 \mu\text{m}^2$ (**Figure S4**) which is beneficial in increasing the overall figure of merit.

When comparing the ZT results of the sintered and post-processed specimens, sulfur infusion significantly enhances the figure of merit (Figure 9d). For the sulfur infusion post-processed samples, a peak ZT value of 1.0 was observed at 780 K. This is the highest figure of merit value ever reported for a 3D printed copper(I) sulfide material at this temperature. The figure of merit results presented in Figure 9d distinctly shows the three-phase transformation zones. From room temperature to around ~370 K, copper(I) sulfide exhibits a monoclinic structure [41] characterized by high electrical conductivity. In the 370-700 K temperature range, samples have a hexagonal crystal structure [42] where copper(I) sulfide is the least efficient. In the temperature range above 700K, there is a phase transition from hexagonal to cubic Cu_2S which has the most desirable properties in terms of thermoelectric performance and stability.

4. Conclusions

This study reports on the use of DIW 3D printing technology to fabricate Cu_{2-x}S samples with high conversion efficiency by introducing the novel sulfur infusion post-processing method. Printed Cu_{2-x}S samples were air cured and then subjected to high-temperature sintering at 1273 K where sulfur is lost to the environment creating a copper-rich alloy and resulting in poor thermoelectric performance. The sulfur infusion process reintroduces the lost sulfur allowing for the reabsorption of the precipitated copper and bringing the Cu/S ratio close to that of the stoichiometric copper(I) sulfide. Reverting the lost sulfur back to the sample significantly enhances the thermoelectric performance of the 3D printed materials. Printed and post-processed Cu_{2-x}S marks electrical conductivity peaking at 143 Scm^{-1} at 750 K, Seebeck coefficient of $175 \mu\text{V/K}$ at 627 K, and thermal conductivity of nearly $0.5 \text{ Wm}^{-1}\text{K}^{-1}$. The culmination of these parameters results in a ZT value of 1.0 at 780 K which is the highest value ever reported for a 3D printed copper(I) sulfide thermoelectric at this temperature.

This work has demonstrated that the loss of sulfur is the key mechanism impairing the thermoelectric properties of additively manufactured Cu_{2-x}S materials. The impaired properties can be reverted to the well-being state by introducing the lost sulfur into the material through an additional post-processing step. ZT was observed to increase nearly five (10) times as a result of the sulfur infusion process. Investigating the sulfur loss on thermoelectric properties of additively manufactured Cu_{2-x}S and introducing a novel remedy for the impaired properties have the potential to greatly impact the thermoelectric industry since it paves the way for the fabrication of environment-friendly, earth-abundant Cu_{2-x}S thermoelectrics with high conversion efficiency and high dimensional freedom.

Supplementary Materials: The following supporting information can be downloaded at the website of this paper posted on Preprints.org. Figure S1: Thermoelectric properties of sulfur infused 3D printed Cu_{2-x}S samples: a) electrical conductivity, b) Seebeck coefficient, and c) figure of merit. Figure S2: Heating profile used for thermoelectric characterization with the Linseis LSR-3 system. Figure S3: Thermal diffusivity a) and specific heat b) of DIW Cu_{2-x}S samples.

Author Contributions: Conceptualization, R.G., W.J.W., G.L.D., D.S., S.S., and E.C.; methodology, R.G., and J.D.; investigation, R.G., W.J.W., and J.D.; writing—original draft preparation, R.G.; writing—review and editing, G.L.D., and E.C.; supervision, E.C.; funding acquisition, D.S. All authors have read and agreed to the published version of the manuscript.

Funding: This work was funded by the U.S. Army Combat Capabilities Development Command Armaments Center under the Project Number DOTC-19-01-INIT0903.

Data Availability Statement: The raw/processed data required to reproduce these findings cannot be shared at this time due to technical or time limitations. All raw data will be made publicly available before the publication of the manuscript.

Conflicts of Interest: The authors declare no conflict of interest.

References

1. Twaha, S., et al., A comprehensive review of thermoelectric technology: Materials, applications, modelling and performance improvement. *Renewable and Sustainable Energy Reviews*, 2016. **65**: p. 698-726.
2. Pourkiaei, S.M., et al., Thermoelectric cooler and thermoelectric generator devices: A review of present and potential applications, modeling and materials. *Energy*, 2019. **186**.
3. Goldsmid, H.J., Bismuth Telluride and Its Alloys as Materials for Thermoelectric Generation. *Materials*, 2014. **7**(4): p. 2577-2592.
4. Poudel, B., et al., High-thermoelectric performance of nanostructured bismuth antimony telluride bulk alloys. *Science*, 2008. **320**(5876): p. 634-638.
5. Witting, I.T., et al., The Thermoelectric Properties of Bismuth Telluride. *Advanced Electronic Materials*, 2019. **5**(6).
6. Yamashita, O., S. Tomiyoshi, and K. Makita, Bismuth telluride compounds with high thermoelectric figures of merit. *Journal of Applied Physics*, 2003. **93**(1): p. 368-374.
7. Zhang, H., et al., Laser additive manufacturing of powdered bismuth telluride. *Journal of Materials Research*, 2018. **33**(23): p. 4031-4039.
8. Dughaish, Z.H., Lead telluride as a thermoelectric material for thermoelectric power generation. *Physica B-Condensed Matter*, 2002. **322**(1-2): p. 205-223.
9. LaLonde, A.D., et al., Lead telluride alloy thermoelectrics. *Materials Today*, 2011. **14**(11): p. 526-532.
10. Pei, Y.Z., et al., Combination of large nanostructures and complex band structure for high performance thermoelectric lead telluride. *Energy & Environmental Science*, 2011. **4**(9): p. 3640-3645.
11. Liu, H., et al., Copper ion liquid-like thermoelectrics. *Nat Mater*, 2012. **11**(5): p. 422-5.
12. Mulla, R. and M.H.K. Rabinal, Copper Sulfides: Earth-Abundant and Low-Cost Thermoelectric Materials. *Energy Technology*, 2019. **7**(7).
13. Oztan, C.Y., et al., Thermoelectric performance of Cu₂Se doped with rapidly synthesized gel-like carbon dots. *Journal of Alloys and Compounds*, 2021. **864**.
14. Kang, S.D., et al., Enhanced stability and thermoelectric figure-of-merit in copper selenide by lithium doping. *Materials Today Physics*, 2017. **1**: p. 7-13.
15. Shi, D.-l., et al., Thermal stability study of Cu_{1.97}Se superionic thermoelectric materials. *Journal of Materials Chemistry C*, 2020. **8**(30): p. 10221-10228.
16. Liu, W.D., et al., Promising and Eco-Friendly Cu₂ X-Based Thermoelectric Materials: Progress and Applications. *Adv Mater*, 2020. **32**(8): p. e1905703.
17. Okamoto, K. and S. Kawai, Electrical Conduction and Phase Transition of Copper Sulfides. *Japanese Journal of Applied Physics*, 1973. **12**.
18. Nieroda, P., et al., Thermoelectric properties of Cu₂S obtained by high temperature synthesis and sintered by IHP method. *Ceramics International*, 2020. **46**(16): p. 25460-25466.
19. Zhao, L., et al., High thermoelectric and mechanical performance in highly dense Cu_{2-x}S bulks prepared by a melt-solidification technique. *Journal of Materials Chemistry A*, 2015. **3**(18): p. 9432-9437.
20. Chakrabarti, D.J. and D.E. Laughlin, The Cu-S (Copper-Sulfur) system. *Bulletin of Alloy Phase Diagrams*, 1983. **4**(3): p. 254-271.
21. He, Y., et al., High thermoelectric performance in non-toxic earth-abundant copper sulfide. *Adv Mater*, 2014. **26**(23): p. 3974-8.
22. Dennler, G., et al., Are Binary Copper Sulfides/Selenides Really New and Promising Thermoelectric Materials? *Advanced Energy Materials*, 2014. **4**(9).
23. Wei, T.-R., et al., Copper chalcogenide thermoelectric materials. *Science China Materials*, 2018. **62**(1): p. 8-24.
24. Li, M., et al., Effect of the Annealing Atmosphere on Crystal Phase and Thermoelectric Properties of Copper Sulfide. *ACS Nano*, 2021. **15**(3): p. 4967-4978.
25. Qiu, P., et al., Suppression of atom motion and metal deposition in mixed ionic electronic conductors. *Nat Commun*, 2018. **9**(1): p. 2910.
26. Oztan, C., et al., Additive manufacturing of thermoelectric materials via fused filament fabrication. *Applied Materials Today*, 2019. **15**: p. 77-82.
27. Burton, M., et al., Printed Thermoelectrics. *Adv Mater*, 2022. **34**(18): p. e2108183.
28. Kim, F., et al., Direct ink writing of three-dimensional thermoelectric microarchitectures. *Nature Electronics*, 2021. **4**(8): p. 579-587.

29. Jo, S., et al., Ink Processing for Thermoelectric Materials and Power-Generating Devices. *Advanced Materials*, 2019. **31**(20).
30. Kato, K., H. Hagino, and K. Miyazaki, Fabrication of Bismuth Telluride Thermoelectric Films Containing Conductive Polymers Using a Printing Method. *Journal of Electronic Materials*, 2013. **42**(7): p. 1313-1318.
31. Amin, A., et al., Screen-printed bismuth telluride nanostructured composites for flexible thermoelectric applications. *Journal of Physics-Energy*, 2022. **4**(2).
32. Chen, B.L., et al., Flexible thermoelectric generators with inkjet-printed bismuth telluride nanowires and liquid metal contacts. *Nanoscale*, 2019. **11**(12): p. 5222-5230.
33. Kim, F., et al., 3D printing of shape-conformable thermoelectric materials using all-inorganic Bi₂Te₃-based inks. *Nature Energy*, 2018. **3**(4): p. 301-309.
34. Burton, M.R., et al., Earth abundant, non-toxic, 3D printed Cu₂-xS with high thermoelectric figure of merit. *Journal of Materials Chemistry A*, 2019. **7**(44): p. 25586-25592.
35. Zheng, Y., et al., High-Temperature Mechanical and Thermoelectric Properties of p-Type Bi_{0.5}Sb_{1.5}Te₃ Commercial Zone Melting Ingots. *Journal of Electronic Materials*, 2013. **43**(6): p. 2017-2022.
36. Ramdohr, P., *The Ore Minerals and Their Intergrowths*. 2013: Elsevier Science.
37. Cook, W.R., *Phase changes in Cu₂S as a function of temperature*. 1972: National Bureau of Standards.
38. Sorokin, G.P. and A.P. Paradenko, *Electrical Properties of Cu₂S*. *Soviet Physics Journal*, 1966.
39. Snyder, G.J. and E.S. Toberer, *Complex thermoelectric materials*. *Nat Mater*, 2008. **7**(2): p. 105-14.
40. Nieroda, P., et al., *Extremely Fast and Cheap Densification of Cu₂S by Induction Melting Method*. *Materials*, 2021. **14**(23).
41. Roseboom, E.H. and JR., *An investigation of the system Cu-S and some natural copper sulfides between 25 and 700 C*. *Economic Geology*, 1966. **61**.
42. Posfai, M. and P.R. Buseck, *Djurleite, digenite, and chalcocite: Intergrowths and transformations*. *American Mineralogist*, 1994. **79**(3-4): p. 308-315.

Disclaimer/Publisher's Note: The statements, opinions and data contained in all publications are solely those of the individual author(s) and contributor(s) and not of MDPI and/or the editor(s). MDPI and/or the editor(s) disclaim responsibility for any injury to people or property resulting from any ideas, methods, instructions or products referred to in the content.